



Article

Polypyrrole Modified MoS₂ Nanorod Composites as Durable Pseudocapacitive Anode Materials for Sodium-Ion Batteries

Miao Jia ^{1,*}, Tong Qi ², Qiong Yuan ², Peizhu Zhao ² and Mengqiu Jia ^{2,*}

¹ College of Chemistry and Materials Engineering, Beijing Technology and Business University, Beijing 100048, China

² Beijing Key Laboratory of Electrochemical Process and Technology for Materials, Beijing University of Chemical Technology, Beijing 100029, China; qitongwork@163.com (T.Q.); 13716673969@163.com (Q.Y.); zhaopzhjy@163.com (P.Z.)

* Correspondence: jiamiao@btbu.edu.cn (M.J.); jiamq@mail.buct.edu.cn (M.J.)

Abstract: As a typical two-dimensional layered metal sulfide, MoS₂ has a high theoretical capacity and large layer spacing, which is beneficial for ion transport. Herein, a facile polymerization method is employed to synthesize polypyrrole (PPy) nanotubes, followed by a hydrothermal method to obtain flower-rod-shaped MoS₂/PPy (FR-MoS₂/PPy) composites. The FR-MoS₂/PPy achieves outstanding electrochemical performance as a sodium-ion battery anode. After 60 cycles under 100 mA g⁻¹, the FR-MoS₂/PPy can maintain a capacity of 431.9 mAh g⁻¹. As for rate performance, when the current densities range from 0.1 to 2 A g⁻¹, the capacities only reduce from 489.7 to 363.2 mAh g⁻¹. The excellent performance comes from a high specific surface area provided by the unique structure and the synergistic effect between the components. Additionally, the introduction of conductive PPy improves the conductivity of the material and the internal hollow structure relieves the volume expansion. In addition, kinetic calculations show that the composite material has a high sodium-ion transmission rate, and the external pseudocapacitance behavior can also significantly improve its electrochemical performance. This method provides a new idea for the development of advanced high-capacity anode materials for sodium-ion batteries.

Keywords: metal sulfide; PPy; pseudocapacitive; sodium-ion battery; anode material



Citation: Jia, M.; Qi, T.; Yuan, Q.; Zhao, P.; Jia, M. Polypyrrole Modified MoS₂ Nanorod Composites as Durable Pseudocapacitive Anode Materials for Sodium-Ion Batteries. *Nanomaterials* **2022**, *12*, 2006. <https://doi.org/10.3390/nano12122006>

Academic Editor: Cheol-Min Park

Received: 12 May 2022

Accepted: 8 June 2022

Published: 10 June 2022

Publisher's Note: MDPI stays neutral with regard to jurisdictional claims in published maps and institutional affiliations.



Copyright: © 2022 by the authors. Licensee MDPI, Basel, Switzerland. This article is an open access article distributed under the terms and conditions of the Creative Commons Attribution (CC BY) license (<https://creativecommons.org/licenses/by/4.0/>).

1. Introduction

With the continuous development of the commercialization of lithium-ion batteries, the scarce lithium resources on Earth can no longer meet the increasing demand for energy storage in the future; therefore, sodium-ion batteries have come into being [1–3]. Sodium belongs to the same group as lithium, thereby having many properties in common with lithium. However, the larger radius of Na⁺ compared to Li⁺ can easily lead to the accelerated crushing of electrode materials in the process of sodiation/desodiation [4,5]. Therefore, the development of suitable anode materials is particularly important.

Recently, two-dimensional layered metal chalcogenides have attracted extensive attention. Park et al. synthesized a variety of metal sulfides/selenides and achieved excellent performance in sodium-ion batteries [6–8]. Metal sulfides have good conductivity and large layer spacing, so they possess high theoretical capacities [9–11]. In addition, layered metal sulfides have unique structural advantages, namely a sandwich-like structure composed of sulfur and metal atoms (M-S-M); the layers are connected by covalent bonds, while each structure is connected by van der Waals force. This kind of structure can ensure rapid sodiation/desodiation [12,13]. Among them, MoS₂ has a larger interlayer spacing (0.62 nm) compared to graphite, which is beneficial to accelerating kinetic processes. Li et al. [14] prepared flower-like MoS₂, which showed remarkable performance in lithium-ion batteries. Kumar et al. [15] explored the binder effect on electrochemical capacity; the obtained MoS₂ microflower presented 595 mAh g⁻¹ under a current density of 50 mA g⁻¹ with a

Na-alginate binder. Yao et al. [16] synthesized grain-like MoS₂ particulates by sulfuring MoO₃; the unique structure could ease volume expansion. Although metal sulfide has its own advantages, there are still factors affecting battery capacity and cycle life, such as its low intrinsic conductivity, repeated electrochemical processes which lead to material structure crushing, formation of a solid electrolyte interface (SEI membrane) causing internal resistance, volume expansion, and so on. In order to solve these problems, researchers have obtained metal sulfide anode materials with good electrochemical properties by making materials at nanometer scale, compounding them with carbon, and designing the spatial structures of these materials [17–21]. Liu et al. [22] designed a type of MoS₂ composite material wrapped in nitrogen-doped 3D hollow carbon framework pores, which can improve the stability of the structure and expose more active sites, such that it showed an excellent electrochemical performance of 413.3 mA h g⁻¹ after 100 cycles at 0.1 A g⁻¹. Wu et al. [23] synthesized Sn/MoS₂@C double-walled hollow nanospheres; this hierarchical structure greatly increased the specific surface area and internal space of the composite materials, which could greatly alleviate the volume expansion of the materials during the charge and discharge processes, such that the composite exhibits excellent long-cycle stability in sodium-ion batteries and still has a capacity of approximately 432 mAh g⁻¹ after 400 cycles at 1 A g⁻¹. Therefore, the structural stability of MoS₂ can be greatly improved through compounding, and the electrochemical performance can be enhanced.

Polypyrrole (PPy) has the advantages of high conductivity, a stable voltage window, environmental friendliness, low toxicity, good thermal stability, and excellent mechanical elasticity [24,25]. It could prevent oxidation of the electrode surface, build a conductive channel in the active electrode materials, and offer reversible redox reactions in the electrochemical processes, thereby attracting wide attention in electrochemical energy storage devices [26–30]. Composite materials of MoS₂ and PPy have been most commonly used in supercapacitors. Tian et al. [31] used a simple method to guide PPy into an ordered molecular structure by in situ forming of MoS₂ nanosheets on a 3D PPy frame, presenting huge application potential in supercapacitors. Hao et al. [32] prepared MoS₂ nanosheets/PPy composites which were deposited on reduced graphene oxide (rGO) through a one-step hydrothermal method. Together, rGO and PPy could effectively improve the conductivity of MoS₂; therefore, the composite material has excellent cycle stability and high energy density. In addition, Wang et al. [33] prepared CNT/MoS₂@PPy composite materials; CNTs and PPy can provide effective ion transport channels, thereby reducing the electrical resistance during cycling and the volume expansion of the material, such that it exhibits excellent performance in lithium-ion batteries. Therefore, it can be expected that materials composed of MoS₂ and PPy should also have broad application prospects in sodium-ion batteries.

Herein, a simple room-temperature polymerization method was used to synthesize PPy nanotubes, followed by a hydrothermal method to obtain the final hollow flower-rod-shaped MoS₂/PPy nanotube composite materials (denoted as FR-MoS₂/PPy). This material is expected to have an ultra-long cycle life and good rate performance.

2. Materials and Methods

2.1. Materials Synthesis

2.1.1. Synthesis of PPy Nanotubes

A combination of 0.243 g of FeCl₃ and 0.049 g of methyl orange was added to 30 mL of deionized water and, after stirring for 0.5 h, 100 μL of pyrrole was added. After stirring for 24 h at room temperature, PPy nanotubes were obtained, which were washed for several times with deionized water and dried in a vacuum oven at 50 °C.

2.1.2. Synthesis of FR-MoS₂/PPy

A combination of 0.1 g of as-prepared PPy nanotubes, 0.300 g of (NH₄)₆Mo₇O₂₄·4H₂O, and 0.885 g of thiourea was stirred under ultrasound for 0.5 h and then added to 30 mL of deionized water. The resulting homogeneous solution was transferred into a 40 mL of Teflon-lined stainless-steel autoclave and heated at 180 °C for 24 h. The black precipitate

was collected and washed several times with deionized water and ethanol, and the sample was dried at 50 °C for 10 h.

2.2. Materials Characterization

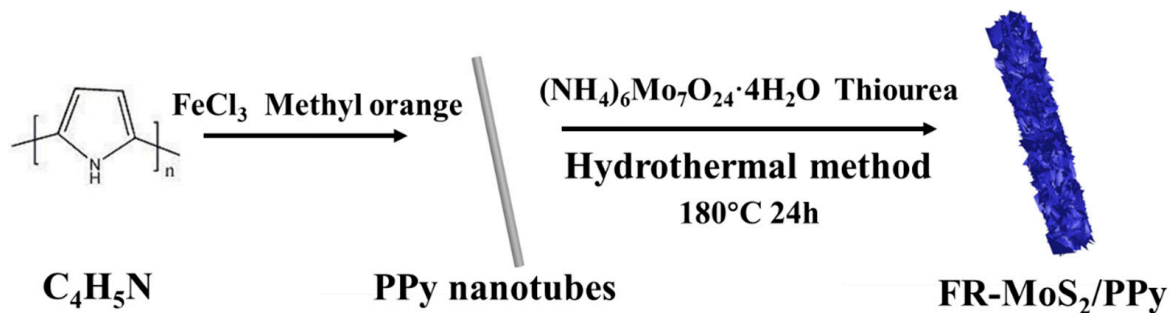
X-ray diffraction (XRD, D/max-2500B2+/PCX, Rigaku, Tokyo, Japan) was used to characterize the crystal structure of the as-prepared FR-MoS₂/PPy, while X-ray photoelectron spectroscopy (XPS, ESCALAB 250, ThermoFisher Scientific, Waltham, MA, USA) was used for element valence analysis. A Fourier transform infrared spectrometer (FTIR, Nicolet iS50, Thermo Nicolet, Ramsey, MN, USA) was used to determine the functional groups of the conductive polymers. The content of MoS₂ in the composite was tested by a thermogravimetric test (TGA, TGA/DSC 1/1100 SF, METTLER, Greifensee, Switzerland) at a temperature range of 25–800 °C. The morphology and element distribution of the composite material were tested by a scanning electron microscope (SEM, Supratm55, ZEISS, Oberkochen, Germany), its internal structure was observed by a transmission electron microscope (TEM, Tecnai G2 F30, FEI, Hillsboro, OR, USA), and the crystal structure of the material was further analyzed by a high-resolution transmission electron microscope (HRTEM, Tecnai G2 F30, FEI, Hillsboro, OR, USA) and a selected-area electron diffraction pattern (SEAD, Tecnai G2 F30, FEI, Hillsboro, OR, USA).

2.3. Electrochemical Measurements

To measure the electrochemical performance of the FR-MoS₂/PPy composite material, a CR2025 coin battery was assembled with sodium as the counter electrode. The as-prepared composite material was mixed with a conductive agent (Super-P) and a binder (sodium alginate) with a ratio of 6:2:2, forming a uniform slurry. The slurry was coated uniformly on the copper foil, and then it was dried thoroughly in a vacuum at 120 °C for more than 10 h. The active-substance loading was about 1 mg cm⁻². The electrolyte used was 1 M sodium perchlorate with 5% FEC dissolved in 1:1 ethylene carbonate and diethyl carbonate; an appropriate amount of FEC additive can not only significantly inhibit the decomposition of electrolyte solvents, but also improve the cycle stability of batteries. The cycle and rate performance were tested by a Neware CT3008 battery test system. Cyclic voltammetry (CV) was tested by a CS350 at different scan rates of 0.1–1 mV s⁻¹, and electrochemical impedance spectroscopy (EIS) was performed at the same electrochemical workstation with a frequency ranging from 100 kHz to 0.01 Hz.

3. Results and Discussion

The preparation process of the FR-MoS₂/PPy composite material is shown in Scheme 1. First, methyl orange and ferric chloride are used to initiate the polymerization of pyrrole monomers into nanotubes at room temperature. Then, the MoS₂ nanosheets grow uniformly on the surface of the PPy nanotubes by a hydrothermal method. Finally, the MoS₂ composite material is obtained.



Scheme 1. Schematic illustration of the synthesis process of FR-MoS₂/PPy.

It can be seen from the XRD pattern (Figure 1a) that the characteristic peaks of MoS₂ before and after compounding with PPy have no significant changes. The peaks at about 16°, 33°, and 57° in the figure correspond to the (0 0 2), (1 0 0), and (1 1 0) crystal planes of MoS₂, respectively, which proves that MoS₂ forms a hexagonal phase structure (JCPDS 77–1716); the existence of the (0 0 2) plane can prove that MoS₂ nanosheets grow uniformly on PPy [34].

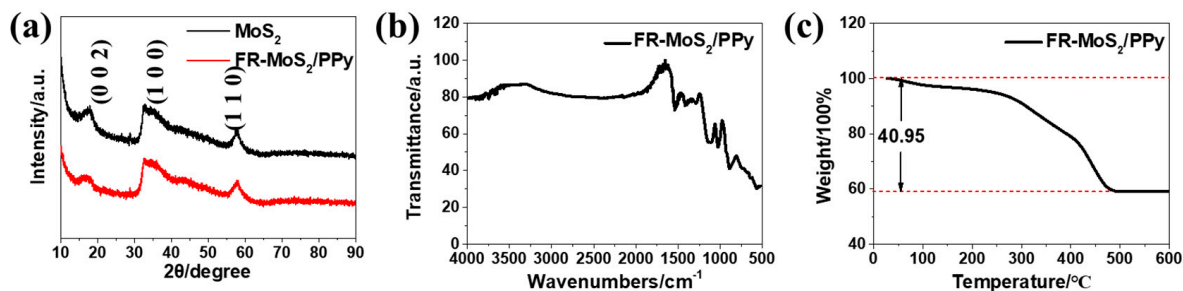


Figure 1. (a) XRD patterns of MoS₂ and FR-MoS₂/PPy, (b) FT-IR spectra, and (c) TGA curve of FR-MoS₂/PPy.

The FT-IR result is presented in Figure 1b; the absorption peak at 1540 cm⁻¹ represents the stretching vibration peak of C-C, the peak at 1400 cm⁻¹ corresponds to the out-of-plane bending vibration peak of C-N, the peak at 1111 cm⁻¹ corresponds to the in-bending vibration peak of =C-H, the peak at 1026 cm⁻¹ corresponds to the in-plane bending vibration peak and out-of-plane bending vibration peak of N-H, the peak at 890 cm⁻¹ corresponds to the out-of-plane bending vibration of =C-H, and the small peak at 1287 cm⁻¹ is related to the doping state of PPy, all of which prove the successful combination of PPy and molybdenum sulfide [32,35,36]. Figure 1c shows the TGA result of FR-MoS₂/PPy. After heating material from room temperature to 800 °C in an air atmosphere, 49.95% of the mass remains. Typically, the reaction of the composite material is as follows: 2MoS₂ + 7O₂ = 2MoO₃ + 4SO₂. Therefore, in addition to the transformation of PPy to CO₂, the mass loss in the TGA curve also includes the SO₂ loss in the reaction of MoS₂, such that the equations can be listed as follows:

$$\frac{W(\text{MoS}_2)}{M(\text{MoS}_2)} = \frac{W(\text{MoO}_3)}{M(\text{MoO}_3)}$$

Among them, $W(\text{MoS}_2)$ and $W(\text{MoO}_3)$ represent the mass fraction of MoS₂ and MoO₃, and $M(\text{MoS}_2)$ and $M(\text{MoO}_3)$ represent the relative molecular masses of MoS₂ and MoO₃; therefore, the content of MoS₂ in the composite material can be calculated as 55.6% [37].

The elemental composition and valence information are tested by XPS. Figure 2a shows the fitting peaks of the Mo element; two peaks at 228.9 and 232.1 eV can be seen, representing Mo 3d_{5/2} and Mo 3d_{3/2}, respectively. They prove that there is Mo⁴⁺ in the composite material, which exists in the form of 1T-MoS₂ in a metastable state with strong metallicity and good conductivity. The two peaks appearing at the higher binding energy area prove that the material contains part of the 2H-MoS₂, which is a proper stable state. Figure 2b shows that the peaks at about 161.7 and 162.9 eV correspond to S 2p_{3/2} and S 2p_{1/2}, respectively, which proves that S²⁻ exists in the composite material. The small peak near 168.7 eV corresponds to the part of the S⁶⁺ has not been fully reduced. Figure 2c shows the peak splitting of C 1s. It can be seen that there are four peaks at about 288.8, 286.4, 285, and 284.2 eV, corresponding to the existence of C-O, C-O-C, C-N, and C-C bonding, respectively. Figure 2d is the total spectrum of the composite material, which further proves the existence of nitrogen in the composite materials [38,39]. The above tests can prove the successful synthesis of the FR-MoS₂/PPy.

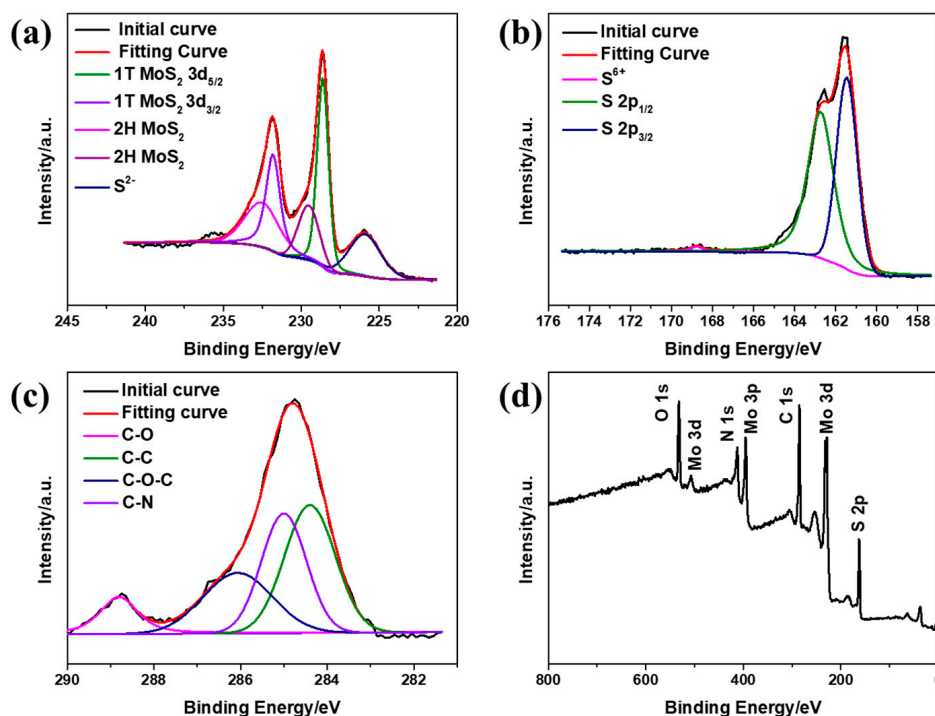
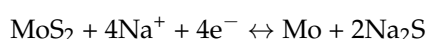


Figure 2. Peak-fitting curve of (a) Mo 3d, (b) S 2p, (c) C 1s, and (d) a survey of FR-MoS₂/PPy.

Figure 3a,b show SEM images of pure MoS₂ at different magnifications. It can be observed that the morphology of pure MoS₂ presents a compact nanoflower structure which has a particle size of about 1 μm and is composed of numerous nanosheets. Figure 3c,d show that, after being compounded with PPy, a large number of MoS₂ nanosheets are grown vertically on the PPy nanotubes, exhibiting a flower-rod morphology with a diameter of about 300 nm. It can be seen that the staggered arrangement of a large number of MoS₂ nanosheets makes the material morphology more dispersed, so it can be expected to increase the specific surface area of the composite material, as well as increase the active sodium storage sites of the composite material and the sodium storage capacity. Figure 3e–h display the EDS mapping analysis of the FR-MoS₂/PPy composites; the elements Mo, S, C, and N can be observed, further verifying the results of the XPS.

It can be seen from the TEM results (Figure 4a,b) that the composite material, with a diameter of about 300 nm, has a hollow structure, with PPy nanotubes inside and MoS₂ nanosheets uniformly coated on the outside. The HRTEM results (Figure 4c) show two different crystal plane spacings of 0.62 and 0.27 nm, corresponding to the two crystal planes (0 0 2) and (1 0 0) of MoS₂, respectively. The SAED pattern (Figure 4d) can be observed showing three clear diffraction rings, corresponding to the three crystal planes (0 0 2), (1 0 0), and (1 1 0) of MoS₂ [40,41].

As shown in Figure 5a, the CV curves of the FR-MoS₂/PPy were measured at a scan rate of 0.1 mV s^{-1} . It can be seen that, during the first cathodic scan, the small reduction peak at 1.1 V corresponds to the beginning stage of the sodium ion insertion among the MoS₂ layers and the formation of the SEI film. The reduction peak at 0.1 V corresponds to the conversion reaction of MoS₂ to Mo [38]. In the anode process, the oxidation peak at about 1.7 V corresponds to the conversion of elemental Mo to MoS₂, which proves the reversibility of the electrode reaction during the electrochemical cycle [16]. In the second cycle, the reaction peak of the electrode shifts slightly, which is due to the polarization phenomenon that cannot be avoided during the battery reaction [42]. The reaction formula can be written as follows [43]:



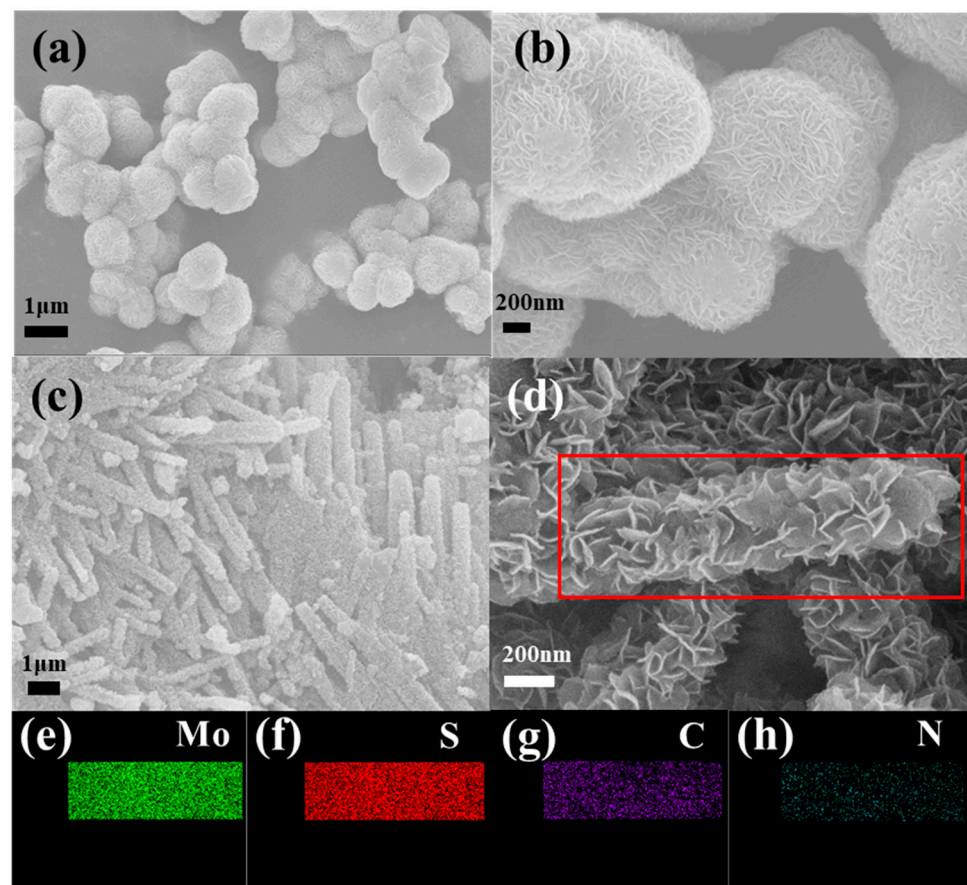


Figure 3. SEM images of (a,b) pure MoS₂ and (c,d) FR-MoS₂/PPy composite; EDS mapping analysis of (e) Mo, (f) S, (g) C, and (h) N.

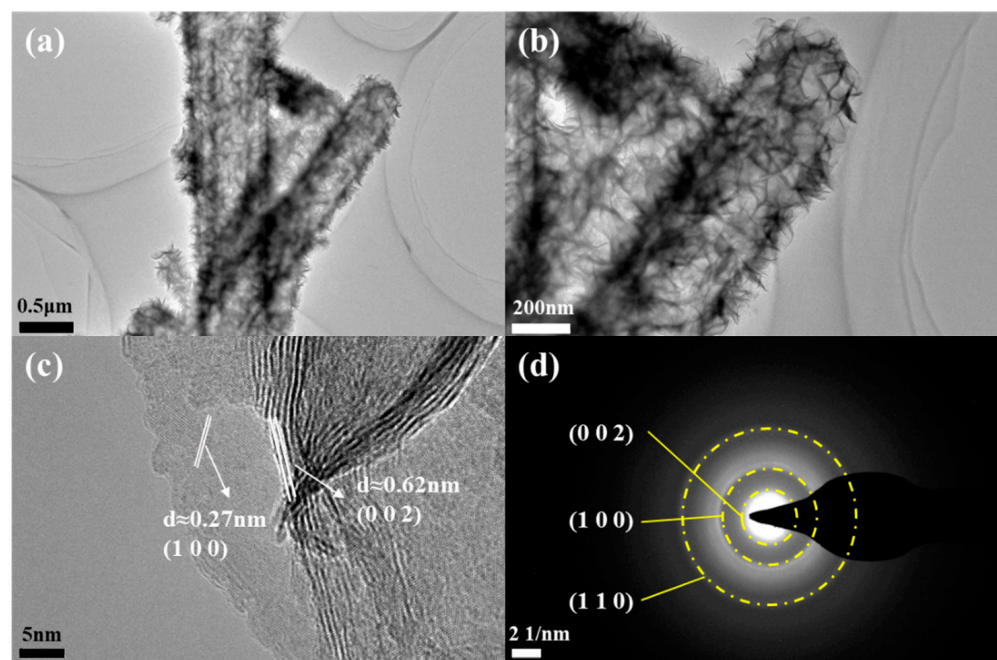


Figure 4. (a,b) TEM images, (c) HRTEM, and (d) SAED pattern of FR-MoS₂/PPy.

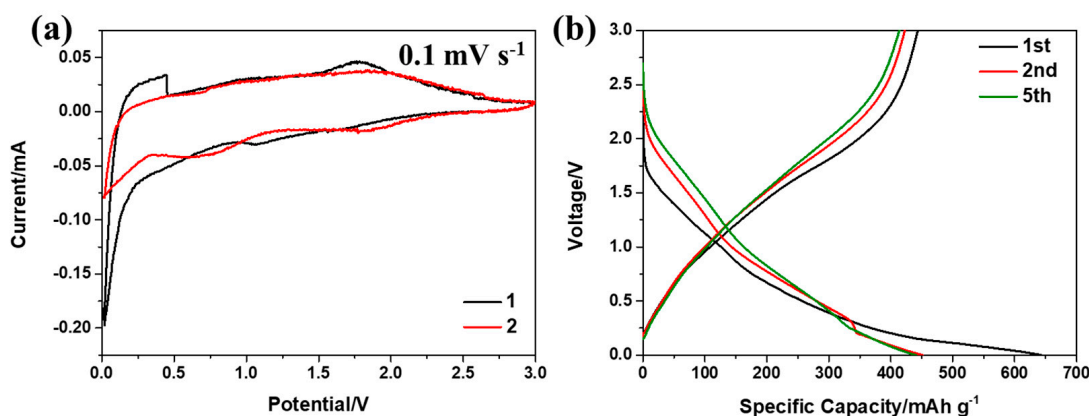


Figure 5. (a) CV curves under a scan rate of 0.1 mV s^{-1} for the first two cycles; (b) charge-discharge curve of 1st, 2nd, 5th cycles at a current density of 100 mA g^{-1} .

Both pure MoS_2 and FR- MoS_2/PPy share the same sodium storage mechanism. As shown in Figure 5b, at a current density of 100 mA g^{-1} , the initial discharge capacity of the FR- MoS_2/PPy composite is 642.7 mAh g^{-1} , and the initial charge capacity is 443.5 mAh g^{-1} . After the second cycle, the discharge curves gradually overlap, indicating that the composite material has excellent cycle stability.

Figure 6 shows the electrochemical performance of pure MoS_2 and FR- MoS_2/PPy composite materials. As shown in Figure 6a, after 60 cycles at a current density of 100 mA g^{-1} , the FR- MoS_2/PPy can still maintain a stable capacity of 431.9 mAh g^{-1} , showing excellent cycle stability, while the capacity of the pure material shows a declining trend, and only a capacity of 58.5 mAh g^{-1} remains after 60 cycles. Figure 6b shows the rate performance; when FR- MoS_2/PPy cycles 10 times under current densities of 0.1, 0.2, 0.5, 1, and 2 A g^{-1} , the capacities are 489.7, 452.8, 416.2, 394.5, and 363.2 mAh g^{-1} , respectively, showing excellent rate performance, and when the current density returns to 0.1 A g^{-1} , the capacity can be stably maintained at 475.2 mAh g^{-1} . However, under the same current density as with FR- MoS_2/PPy , the rate performance of the pure material is relatively inferior, maintaining capacities of only 168.7, 133.5, 90.7, 66.0, and 47.4 mAh g^{-1} , and when the current density returns to 0.1 mA g^{-1} , the capacity can only reach 94.7 mAh g^{-1} . The cycle stability of the two materials was also tested under a relatively high current (500 mA g^{-1}); as shown in Figure 6c, FR- MoS_2/PPy and pure MoS_2 can maintain 386.9 and 27.4 mAh g^{-1} after 150 cycles, respectively. The above results show that the compounding with PPy helps MoS_2 gain higher capacity and more stable performance than pure MoS_2 , which could benefit from the synergistic effect between the two compounds and the enhanced electrochemical performance brought by PPy.

The EIS test is performed after 20 cycles under a current density of 200 mA g^{-1} ; the fitting results can be used to judge the improvement of the electroconductivity and charge transfer rate of the composite. As shown in Figure 7a, the impedance curves of MoS_2 and FR- MoS_2/PPy are both made up of semicircles and inclined straight lines, indicating that the electrochemical kinetics of the materials can be divided into two steps. First, sodium ions migrate through the electrolyte to reach the vicinity of the electrode surface, such that the external circuit transfers electrons to the electrode surface to maintain charge balance. In this period, the semicircle of the EIS represents the formation of SEI layer impedance (R_f), charge transfer impedance (R_{ct}), and double capacitance impedance (C). Then, a large amount of sodium ions can accumulate on the electrode surface. Therefore, the Na^+ concentration on the electrode surface becomes much higher than that of the interior. The resulting Na^+ concentration gradient can cause sodium ions to diffuse from the electrode surface to the interior to maintain balance. This process produces a diffusion impedance, called “Warburg impedance” (W_s), which can be reflected by the slash part of the EIS results. In addition, R_e represents the impedance of the battery, which can be reflected in the intercept of the high-frequency region Z' [44]. The fitting results of R_e , R_f ,

and R_{ct} for the MoS_2 and FR- MoS_2 /PPy electrodes are shown in Table 1. It can be clearly seen that the R_{ct} values of MoS_2 and FR- MoS_2 /PPy are 105.60 and 75.06 Ω , respectively. The charge transfer resistance of FR- MoS_2 /PPy is significantly reduced compared to that of pure MoS_2 , owing to the introduction of PPy increasing the electronic conductivity of composite material, which is beneficial to improving the electrochemical performance of material. Table 2 shows the electrochemical performance comparison of different MoS_2 composite materials.

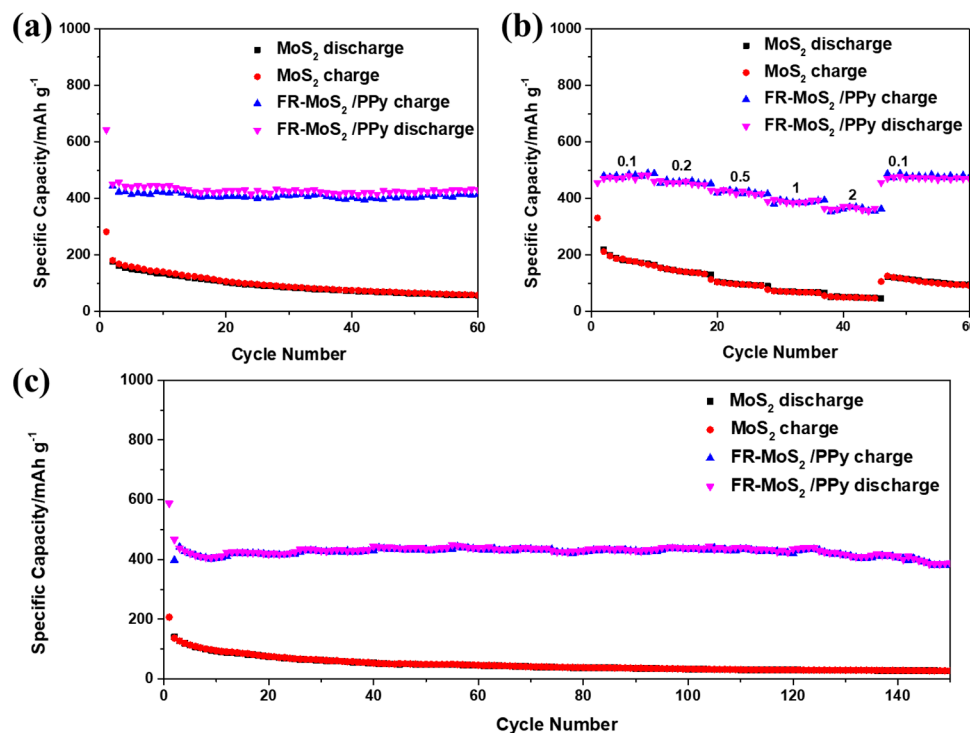


Figure 6. (a) Cycle performance under 100 mA g^{-1} , (b) rate performance, and (c) cycle performance under 500 mA g^{-1} of MoS_2 and FR- MoS_2 /PPy.

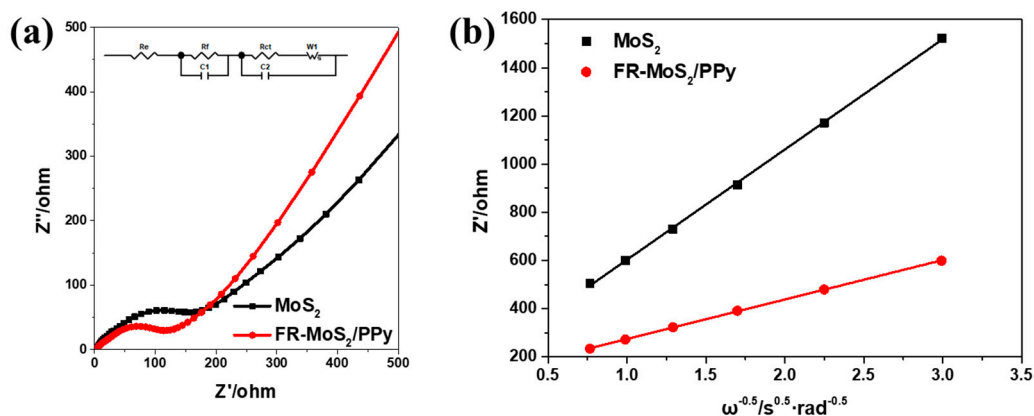


Figure 7. (a) EIS plots of MoS_2 and FR- MoS_2 /PPy after 20 cycles under 200 mA g^{-1} , (b) Z' vs. $\omega^{-0.5}$ plots calculated from EIS under low frequency.

Table 1. EIS fitting results of MoS_2 and FR- MoS_2 /PPy.

Samples	R_e/Ω	R_f/Ω
MoS_2	5.13	25.14
FR- MoS_2 /PPy	5.54	18.46

Table 2. Comparison of different MoS₂ anode materials in sodium-ion batteries.

Samples	Current Density (mA g ⁻¹)	Cycle Number	Capacity (mAh g ⁻¹)	Reference
MoS ₂ microflowers	100	50	595	[15]
G-MoS ₂	500	300	312	[16]
MoS ₂ hollow spheres	100	100	391.4	[17]
FR-MoS ₂ /PPy	100	60	431.9	This Work
	500	150	386.9	

In addition, the fitting results in the low-frequency region can be used to calculate the diffusion coefficient (D_{Na^+}) of Na⁺, and the calculation equations can be written as follows [45,46]:

$$Z' = R_e + R_{ct} + \sigma\omega^{-0.5}$$

$$D_{\text{Na}^+} = \frac{(RT)^2}{2\left(\text{An}^2\text{F}^2\text{C}\sigma\right)^2}$$

Among them, R represents the ideal gas constant with a value of 8.314, T represents the absolute temperature in Kelvin, with a value of 298.15 K, and n represents the number of electrons transferred in the electrochemical process. F is the Faraday constant with a value of 96,500 C mol⁻¹. C is the sodium ion concentration. Ω stands for the angular frequency and σ represents the Warburg factor, which can be calculated from Z' fitting. Figure 7b shows the $Z'-\omega^{-0.5}$ graph. The sodium diffusion coefficients of the MoS₂ and FR-MoS₂/PPy are 7.23×10^{-11} and 1.07×10^{-10} cm² s⁻¹, respectively, indicating that FR-MoS₂/PPy has a higher ion transfer rate.

In order to further study the characteristics of the sodium storage processes of the FR-MoS₂/PPy electrode, the CV curves were tested under scan rates ranging from 0.2 to 1 mV s⁻¹ (Figure 8a). The following equation can express the relationship between Log (scan rate, mV s⁻¹) and Log (peak current, A):

$$i = av^b$$

$$\text{Log}(i) = b\text{Log}(v) + \text{Log}(a)$$

In the above formula, when the b value is close to 0.5, ion diffusion determines the electrochemical reaction, and when the b value is close to 1, it is mainly controlled by the pseudocapacitance process [46,47]. The linear relationship between Log (i) and Log (v) is shown in Figure 8b. The corresponding b values of the two main redox peaks are 0.91074 for the anode and 0.94115 for the cathode, respectively, which indicates that the redox process of the FR-MoS₂/PPy composite includes partial pseudocapacitive performance, leading to its relatively remarkable rate performance. The total current at a fixed potential includes the pseudocapacitance mechanism (k_1v) and the ion diffusion process ($k_2v^{1/2}$), which can be calculated by the following formula:

$$i = k_1v + k_2v^{1/2}$$

Here, k_1v and $k_2v^{1/2}$ represent the pseudocapacitance process and the diffusion-controlled Na⁺ insertion–extraction, respectively [48]. Figure 8c shows the ratio of the pseudocapacitance process at a scanning speed of 0.8 mV s⁻¹. It can be seen that the ratio of the pseudocapacitance contribution is about 80.4% (green shaded area). Figure 8d shows that the contribution rates of the pseudocapacitance were 67.5%, 76%, 78.5%, 80.4%, and 82.8% at different scanning speeds of 0.2, 0.4, 0.6, 0.8, and 1 mV s⁻¹. This means that, as the scanning speed increases, the contribution of the pseudocapacitance gradually accounts for more of the total capacitance.

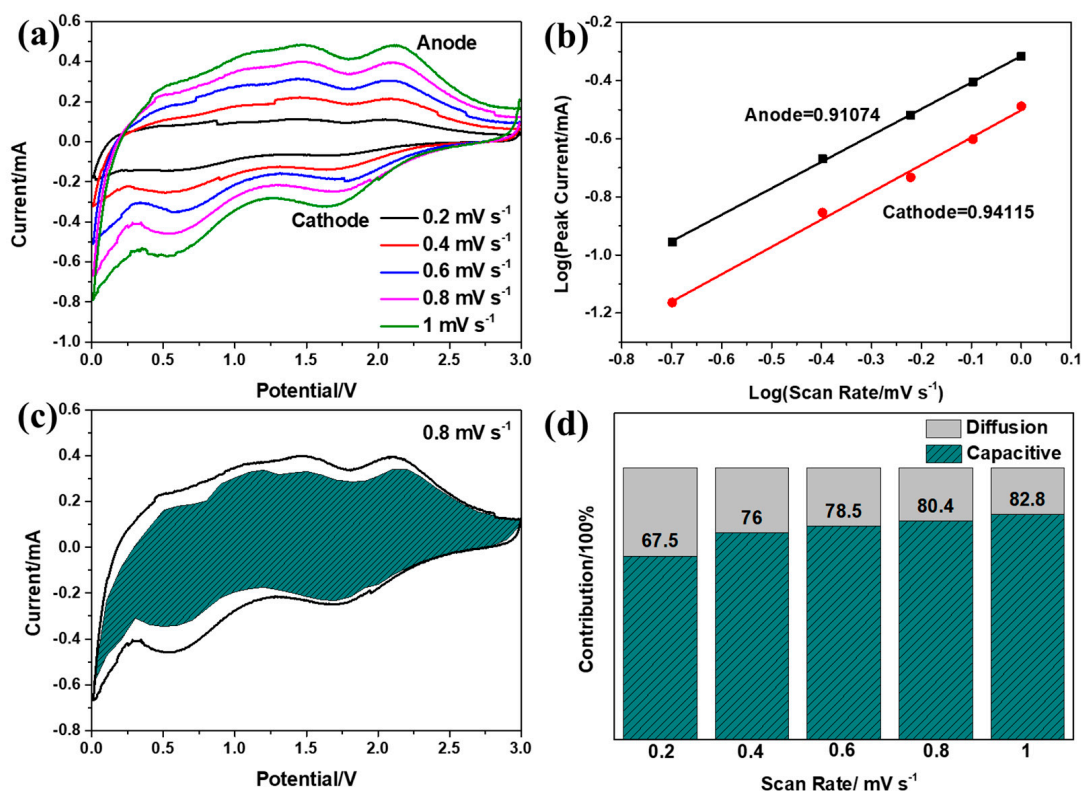


Figure 8. (a) The second-cycle CV curves of the FR-MoS₂/PPy electrode under different scan rates, ranging from 0.2 to 1 mV s⁻¹; (b) the slope of the fitted curve of Log (scan rate) and Log (peak current); (c) the proportion of the pseudocapacitance contribution during the electrochemical process when the scan rate is 0.8 mV s⁻¹; (d) proportion of the pseudocapacitance contribution at different scan rates.

4. Conclusions

Herein, a hollow MoS₂/PPy composite material with flower-rod morphology (FR-MoS₂/PPy) was successfully synthesized through a two-step method. The as-prepared material obtained outstanding performance in electrochemical tests. Under a current density of 100 mA g⁻¹, the FR-MoS₂/PPy can maintain a capacity of 431.9 mAh g⁻¹ after 60 cycles, and even under a high density of 2 A g⁻¹, the composite can still reach a high capacity of 363.2 mAh g⁻¹. The excellent electrochemical performance can be attributed to the synergistic effect between the different components of the composite material. The hollow structure also relieves the volume expansion of the material during the deintercalation of the sodium. In addition, the dispersed MoS₂ nanosheets can increase the specific surface area of the material, to a certain extent, and increase the active sites of sodium storage. Furthermore, the pseudocapacitance characteristics can effectively increase the energy density of the electrode material so as to obtain excellent rate performance.

Author Contributions: Conceptualization, M.J. (Miao Jia); data curation, M.J. (Miao Jia); funding acquisition, M.J. (Miao Jia); methodology, T.Q.; project administration, M.J. (Miao Jia); resources, P.Z.; supervision, M.J. (Mengqiu Jia); writing—original draft, M.J. (Miao Jia) and Q.Y.; writing—review and editing, Q.Y. and M.J. (Mengqiu Jia). All authors have read and agreed to the published version of the manuscript.

Funding: This research was funded by the Research Foundation for Youth Scholars of Beijing Technology and Business University (QNJJ2021-22).

Data Availability Statement: The data presented in this study are available upon request from the corresponding author.

Conflicts of Interest: The authors declare no conflict of interest.

References

1. Li, Y.; Han, M.; Zhou, Z.; Xia, X.; Chen, Q.; Chen, M. Topological Insulator-Assisted MoSe₂/Bi₂Se₃ Heterostructure: Achieving Fast Reaction Kinetics Toward High Rate Sodium-Ion Batteries. *ChemElectroChem* **2021**, *8*, 697–704. [[CrossRef](#)]
2. Lim, Y.; Li, X.; Yang, H. Recent Tactics and Advances in the Application of Metal Sulfides as High-Performance Anode Materials for Rechargeable Sodium-Ion Batteries. *Adv. Funct. Mater.* **2021**, *31*, 2006761. [[CrossRef](#)]
3. Zhou, C.; Zhang, P.; Liu, J.; Zhou, J.; Wang, W.; Li, K.; Wu, J.; Lei, Y.; Chen, L. Hierarchical NiCo₂Se₄ nanoneedles/nanosheets with N-doped 3D porous graphene architecture as free-standing anode for superior sodium ion batteries. *J. Colloid Interface Sci.* **2021**, *587*, 260–270. [[CrossRef](#)] [[PubMed](#)]
4. Men, S.; Lin, J.; Zhou, Y.; Kang, X. N-doped porous carbon wrapped FeSe₂ nanoframework prepared by spray drying: A potential large-scale production technique for high-performance anode materials of sodium ion batteries. *J. Power Source* **2021**, *485*, 229310. [[CrossRef](#)]
5. Wu, Y.; Wang, Y.; Shao, S.i.; Ma, Y.; Zhang, J.; Kang, W.; Xu, J. Transformation of Two-Dimensional Iron Sulfide Nanosheets from FeS₂ to FeS as High-Rate Anodes for Pseudocapacitive Sodium Storage. *ACS Appl. Energy Mater.* **2020**, *3*, 12672–12681. [[CrossRef](#)]
6. Park, J.; Kang, Y. Multicomponent (Mo, Ni) metal sulfide and selenide microspheres with empty nanovoids as anode materials for Na-ion batteries. *J. Mater. Chem. A* **2017**, *5*, 8616–8623. [[CrossRef](#)]
7. Park, J.; Park, G.; Kang, Y. Exploration of cobalt selenite–carbon composite porous nanofibers as anode for sodium-ion batteries and unveiling their conversion reaction mechanism. *J. Mater. Sci. Technol.* **2021**, *89*, 24–35. [[CrossRef](#)]
8. Park, J.; Lee, A.; Park, G.; Kang, Y. Synthesis of MnSe@C yolk-shell nanospheres via a water vapor-assisted strategy for use as anode in sodium-ion batteries. *Int. J. Energy Res.* **2022**, *46*, 2500–2511. [[CrossRef](#)]
9. Li, H.; Ma, Y.; Zhang, H.; Diemant, T.; Behm, R.; Varzi, A.; Passerini, S. Metal–Organic Framework Derived Fe₇S₈ Nanoparticles Embedded in Heteroatom-Doped Carbon with Lithium and Sodium Storage Capability. *Small* **2020**, *4*, 2000637. [[CrossRef](#)]
10. Dogrusoz, M.; Cakan, R. Mechanochemical synthesis of SnS anodes for sodium ion batteries. *Energy Res.* **2020**, *44*, 10809–10820. [[CrossRef](#)]
11. Zhao, Z.; Li, S.; Li, C.; Liu, Z.; Li, D. Hollow CoS₂@C nanocubes for high-performance sodium storage. *Appl. Surf. Sci.* **2020**, *519*, 146268. [[CrossRef](#)]
12. Xiao, Y.; Lee, S.; Sun, Y. The Application of Metal Sulfides in Sodium Ion Batteries. *Adv. Energy Mater.* **2017**, *7*, 1601329. [[CrossRef](#)]
13. Huang, Y.; Xiong, D.; Li, X.; Sari, H.; Peng, J.; Li, Y.; Li, Y.; Li, D.; Sun, Q.; Sun, X. Recent Advances of Bimetallic Sulfide Anodes for Sodium Ion Batteries. *Front. Chem.* **2020**, *8*, 353. [[CrossRef](#)] [[PubMed](#)]
14. Li, J.; Wang, D.; Ma, H.; Li, M.; Pan, Z.; Jiang, Z.Y. Tian, Ionic liquid assisted hydrothermal synthesis of MoS₂ double-shell polyhedral cages with enhanced catalytic hydrogenation activities. *RSC Adv.* **2017**, *7*, 23523–23529. [[CrossRef](#)]
15. Kumar, P.; Jung, Y.; Kim, D. High performance of MoS₂ microflowers with a water-based binder as an anode for Na-ion batteries. *RSC Adv.* **2015**, *5*, 79845–79851. [[CrossRef](#)]
16. Yao, K.; Xu, Z.; Li, Z.; Liu, X.; Shen, X.; Cao, L.; Huang, J. Synthesis of Grain-like MoS₂ for High-Performance Sodium-Ion Batteries. *ChemSusChem* **2018**, *11*, 2130–2137. [[CrossRef](#)]
17. Wang, J.; Han, L.; Li, X.; Zeng, L.; Wei, M. MoS₂ hollow spheres in ether-based electrolyte for high performance sodium ion battery. *J. Colloid Interface Sci.* **2019**, *548*, 20–24. [[CrossRef](#)]
18. Fan, B.; Fan, H.; Chen, X.; Gao, X.; Chen, S.; Tang, Q.; Luo, W.; Deng, Y.; Hu, A.; Hu, W. Metallic-State MoS₂ Nanosheets with Atomic Modification for Sodium Ion Batteries with a High Rate Capability and Long Lifespan. *ACS Appl. Mater. Interfaces* **2021**, *13*, 19894–19903. [[CrossRef](#)]
19. Meng, A.; Huang, T.; Li, H.; Cheng, H.; Lin, Y.; Zhao, J.; Li, Z. Sulfur vacancies and morphology dependent sodium storage properties of MoS_{2-x} and its sodiation/desodiation mechanism. *J. Colloid Interface Sci.* **2021**, *589*, 147–156. [[CrossRef](#)]
20. Yue, X.; Wang, J.; Patil, A.; An, X.; Xie, Z.; Hao, X.; Jiang, Z.; Abudula, A.; Guan, G. A novel vanadium-mediated MoS₂ with metallic behavior for sodium ion batteries: Achieving fast Na⁺ diffusion to enhance electrochemical kinetics. *Chem. Eng. J.* **2021**, *417*, 128107. [[CrossRef](#)]
21. He, C.; Yin, W.; Li, X.; Zheng, J.; Tang, B.; Rui, Y. Molybdenum disulfide synthesized by molybdenum-based metal organic framework with high activity for sodium ion battery. *Electrochim. Acta* **2021**, *365*, 137353. [[CrossRef](#)]
22. Liu, M.; Chen, S.; Jin, Y.; Fang, Z. MoS₂ encapsulated in three-dimensional hollow carbon frameworks for stable anode of sodium ion batteries. *CrystEngComm* **2021**, *23*, 5214–5225. [[CrossRef](#)]
23. Wu, X.; Wu, H.; Xie, B.; Wang, R.; Wang, J.; Wang, D.; Shi, Q.; Diao, G.; Chen, M. Atomic Welded Dual-Wall Hollow Nanospheres for Three-in-One Hybrid Storage Mechanism of Alkali Metal Ion Batteries. *ACS Nano* **2021**, *15*, 14125–14136. [[CrossRef](#)]
24. Dai, Z.; Ke, H.; Long, Z.; Li, R.; Shi, C.; Su, X.; Qiao, H.; Wang, K.; Liu, K. Facile synthesis and high lithium storage properties of mesoporous polypyrrole coated CoFe₂O₄ nanofibers. *J. Alloys Compd.* **2021**, *858*, 158324. [[CrossRef](#)]
25. Jyothibasu, J.; Kuo, D.; Lee, R. Flexible and freestanding electrodes based on polypyrrole/carbon nanotube/cellulose composites for supercapacitor application. *Cellulose* **2019**, *26*, 4495–4513. [[CrossRef](#)]
26. Li, Q.; Jiao, Q.; Zhou, W.; Feng, X.; Shi, Q.; Dai, Z.; Gu, T.; Zhao, Y.; Li, H.; Feng, C. Controllable construction of core–shell CuCo₂S₄@polypyrrole nanocomposites as advanced anode materials for high-performance sodium ion half/full batteries. *Mater. Chem. Front.* **2021**, *5*, 293–303. [[CrossRef](#)]
27. Fang, Y.; Yu, X.; Lou, X. Formation of Polypyrrole-Coated Sb₂Se₃ Microclips with Enhanced Sodium-Storage Properties. *Angew. Chem. Int. Ed.* **2018**, *57*, 9859–9863. [[CrossRef](#)]

28. He, Q.; Rui, K.; Chen, C.; Yang, J.; Wen, Z. Interconnected CoFe₂O₄-Polypyrrole Nanotubes as Anode Materials for High Performance Sodium Ion Batteries. *ACS Appl. Mater. Interfaces* **2017**, *9*, 36927–36935. [[CrossRef](#)]
29. Liao, Q.; Hou, H.; Duan, J.; Liu, S.; Yao, Y.; Dai, Z.; Yu, C.; Li, D. Composite sodium p-toluenesulfonate/polypyrrole/TiO₂ nanotubes/Ti anode for sodium ion battery. *Int. J. Hydrogen Energy* **2017**, *42*, 12414–12419. [[CrossRef](#)]
30. Wang, B.; Li, Y.; Han, L.; Liu, K.; Hao, B.; Wu, X. Soft-templated synthesis of core-shell heterostructured Ni₃S₂@polypyrrole nanotube aerogels as anode materials for high-performance lithium ion batteries. *New J. Chem.* **2021**, *45*, 13127–13136. [[CrossRef](#)]
31. Tian, Y.; Liu, J.; Song, X.; Zhao, L.; Zhang, P.; Gao, L. Interface guide: In-situ integrating MoS₂ nanosheets into highly ordered polypyrrole film for high performance flexible supercapacitor electrodes. *Compos. Sci. Technol.* **2020**, *197*, 108263. [[CrossRef](#)]
32. Hao, J.; Liu, H.; Han, S.; Lian, J. MoS₂ Nanosheet-Polypyrrole Composites Deposited on Reduced Graphene Oxide for Supercapacitor Applications. *ACS Appl. Nano Mater.* **2021**, *4*, 1330–1339. [[CrossRef](#)]
33. Wang, J.; Sun, L.; Gong, Y.; Wu, L.; Sun, C.; Zhao, X.; Shi, X.; Lin, Y.; Wang, K.; Zhang, Y. A CNT/MoS₂@PPy composite with double electron channels and boosting charge transport for high-rate lithium storage. *Appl. Surf. Sci.* **2021**, *566*, 150693. [[CrossRef](#)]
34. Lei, J.; Lu, X.; Nie, G.; Jiang, Z.; Wang, C. One-Pot Synthesis of Algae-Like MoS₂/PPy Nanocomposite: A Synergistic Catalyst with Superior Peroxidase-Like Catalytic Activity for H₂O₂ Detection. *Part. Part. Syst. Charact.* **2015**, *32*, 886–892. [[CrossRef](#)]
35. Casamachin, D.; Rosa, J.; Ortiz, C.; Rio, D.; Vargas, D.; Escamilla, G.; Guzman, N.; Medina, V.; Velazquez, E. Visible-light photocatalytic degradation of acid violet 7 dye in a continuous annular reactor using ZnO/PPy photocatalyst: Synthesis, characterization, mass transfer effect evaluation and kinetic analysis. *Chem. Eng. J.* **2019**, *373*, 325–337. [[CrossRef](#)]
36. Chen, Y.; Ma, W.; Cai, K.; Yang, X.; Huang, C. In Situ Growth of Polypyrrole onto Three-Dimensional Tubular MoS₂ as an Advanced Negative Electrode Material for Supercapacitor. *Electrochim. Acta* **2017**, *246*, 615–624. [[CrossRef](#)]
37. Zhang, Z.; Shi, X.; Yang, X. Synthesis of core-shell NiSe/C nanospheres as anodes for lithium and sodium storage. *Electrochim. Acta* **2016**, *208*, 238–243. [[CrossRef](#)]
38. Geng, X.; Jiao, Y.; Han, Y.; Mukhopadhyay, A.; Yang, L.; Zhu, H. Freestanding Metallic 1T MoS₂ with Dual Ion Diffusion Paths as High Rate Anode for Sodium-Ion Batteries. *Adv. Funct. Mater.* **2017**, *27*, 1702998. [[CrossRef](#)]
39. Yu, H.; Wang, Z.; Ni, J.; Li, L. Freestanding nanosheets of 1T-2H hybrid MoS₂ as electrodes for efficient sodium storage. *J. Mater. Sci. Technol.* **2021**, *67*, 237–242. [[CrossRef](#)]
40. Zhu, Y.; Li, H.; Wu, Y.; Yang, L.; Sun, Y.; Chen, G.; Liu, Y.; Wu, Z.; Zhang, C.; Guo, X. Unveiling the abnormal capacity rising mechanism of MoS₂ anode during long-term cycling for sodium-ion batteries. *RSC Adv.* **2021**, *11*, 28488–28495. [[CrossRef](#)]
41. Wang, T.; Xi, Q.; Wang, K.; Zeng, Z.; Du, Z.; Xu, Z.; Xie, L.; Ai, W.; Huang, W. Covalently binding ultrafine MoS₂ particles to N, S co-doped carbon renders excellent Na storage performances. *Carbon* **2021**, *184*, 177–185. [[CrossRef](#)]
42. Jia, M.; Jin, Y.; Zhao, C.; Zhao, P.; Jia, M. ZnSe nanoparticles decorated with hollow N-doped carbon nanocubes for high-performance anode material of sodium ion batteries. *J. Alloys Compd.* **2020**, *831*, 154749. [[CrossRef](#)]
43. Wang, S.; Cao, F.; Li, Y.; Zhang, Z.; Zhou, D.; Yang, Y.; Tang, Z. MoS₂-Coupled Carbon Nanosheets Encapsulated on Sodium Titanate Nanowires as Super-Durable Anode Material for Sodium-Ion Batteries. *Adv. Sci.* **2019**, *6*, 1900028. [[CrossRef](#)] [[PubMed](#)]
44. Li, H.; Yu, K.; Fu, H.; Guo, B.; Lei, X.; Zhu, Z. MoS₂/Graphene Hybrid Nanoflowers with Enhanced Electrochemical Performances as Anode for Lithium-Ion Batteries. *J. Phys. Chem. C* **2015**, *119*, 7959–7968. [[CrossRef](#)]
45. Ren, W.; Zhou, W.; Zhang, H.; Cheng, C. ALD TiO₂-Coated Flower-like MoS₂ Nanosheets on Carbon Cloth as Sodium Ion Battery Anode with Enhanced Cycling Stability and Rate Capability. *ACS Appl. Mater. Interfaces* **2017**, *9*, 487–495. [[CrossRef](#)] [[PubMed](#)]
46. Guan, S.; Wang, T.; Fu, X.; Fan, L.; Peng, Z. Coherent SnS₂/NiS₂ hetero-nanosheet arrays with fast charge transfer for enhanced sodium-ion storage. *Appl. Surf. Sci.* **2020**, *508*, 145241. [[CrossRef](#)]
47. Fang, G.; Wu, Z.; Zhou, J.; Zhu, C.; Cao, X.; Lin, T.; Chen, Y.; Wang, C.; Pan, A.; Liang, S. Observation of Pseudocapacitive Effect and Fast Ion Diffusion in Bimetallic Sulfides as an Advanced Sodium-Ion Battery Anode. *Adv. Energy Mater.* **2018**, *8*, 1703155. [[CrossRef](#)]
48. Lu, Z.; Wang, N.; Zhang, Y.; Xue, P.; Guo, M.; Tang, B.; Bai, Z.; Dou, S. Pyrite FeS₂@C nanorods as smart cathode for sodium ion battery with ultra-long lifespan and notable rate performance from tunable pseudocapacitance. *Electrochim. Acta* **2018**, *260*, 755–761. [[CrossRef](#)]